Supplementary Information for

Strong charge concentration polarization induced by cross-conjugated system of imide-linked porous organic polymers for efficient photocatalytic H_2O_2 production

Xiaojuan Bai*[a,b], Yihan Cao[b], Dailu Zhang[b], Chi Zhang[b]

[a] Key Laboratory of Urban Stormwater System and Water Environment, Ministry of Education, Beijing University of Civil Engineering and Architecture, Beijing 100044, China. E-mail: baixiaojuan@bucea.edu.cn

[b] Beijing Energy Conservation & Sustainable Urban and Rural Development Provincial and Ministry Co-construction Collaboration Innovation Center, Beijing University of Civil Engineering and Architecture, Beijing, China.

E-mail: baixiaojuan@bucea.edu.cn (Xiaojuan Bai)

Experimental procedures

Supplementary Text 1. Experimental Section

A 0.1 mmol quantity of HPMDA/PMDA and TAPB was dispersed in a solution comprising 4 mL 1,3,5-trimethylbenzene, 2 mL N-methylpyrrolidone (NMP), and 3 mL isoquinoline, then subjected to 30 minutes of ultrasonication. The reaction was conducted under microwave irradiation at 160 °C for 2 hours. The synthesis of TAPB-PMDA follows the previously reported procedure for synthesizing amide-linked porous polymers, but the synthesis method has been optimized[1]. The microwave-assisted condition significantly reduces the reaction time compared to conventional solvothermal methods (typically 3–5 days) while maintaining high conversion efficiency. The system was cooled to room temperature after completion, and the product was isolated via centrifugation. The supernatant was discarded, and the solid was washed cyclically three times with ultra-pure water, ethanol, and anhydrous tetrahydrofuran (THF), respectively. The pale yellow powder was dried under vacuum at 80 °C for 12 hours (Scheme S1).

In this experiment, 5 mg of catalyst was evenly mixed into 25 mL of ultrapure water. After ultrasonication for 5 minutes, magnetic stirring was performed for 30 minutes under dark conditions to reach adsorption equilibrium. A 1-hour photocatalytic experiment was performed using a xenon lamp, with samples taken at 10-minute intervals. Samples were filtered using a membrane, and the H_2O_2 content was measured via iodometry. Finally, quantitative analysis was performed using an ultraviolet spectrophotometer at 350 nm. In the CIP degradation study, 5 ppm of CIP was introduced to examine the impact of coexisting anions, such as sulfate (SO_4^{2-}), bicarbonate (HCO_3^-), and chloride (Cl^-), on its photocatalytic degradation. Tap and lake water samples were collected to assess the material's applicability in real water matrices.

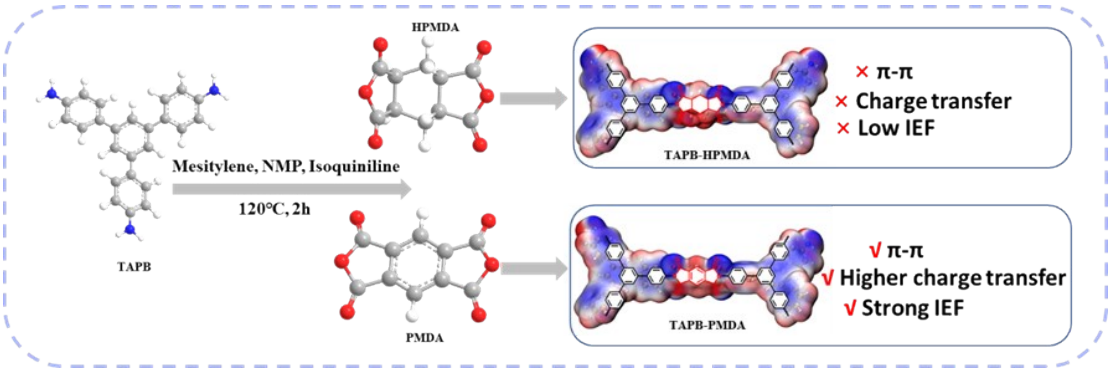

Scheme 1. Schematic illustration of the synthetic chemical structures of TAPB-HPMDA and TAPB-PMDA

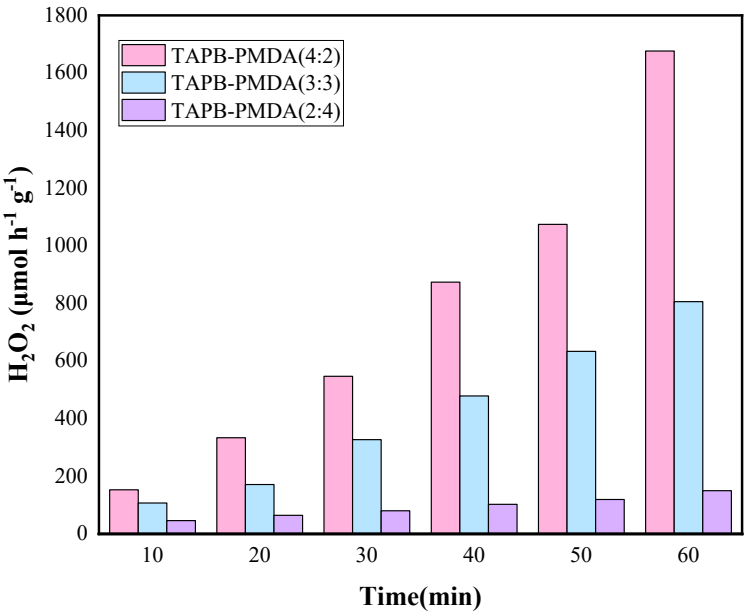

The samples were prepared by tuning the solvent ratio during material synthesis. Three distinct samples were synthesized using 1,3,5-trimethylbenzene: NMP volume ratios of 4:2, 3:3, and 2:4, respectively. Photocatalytic hydrogen peroxide production was evaluated for all samples, revealing that the TAPB–PMDA sample fabricated at the 1,3,5-trimethylbenzene: NMP ratio of 4:2 exhibited the highest photocatalytic activity. Consequently, this optimally performing sample was selected for subsequent experiments.

Supplementary Text 2. Characterization of photocatalysts

The optical bandgap (E_g) was calculated according to the following equation:

$$(\alpha \cdot h\vartheta)^{1/n} = B(h\vartheta - E_g)$$

Where α is the adsorption coefficient, h is the Planck constant, ν is the light frequency, B is a constant, and E_g is the corresponding bandgap. In addition, the n factor is determined by the nature of the electron transition. Particularly, n = 1/2 means a direct bandgap transition, and n=2 suggests an indirect bandgap transition. In this work, the value of n for POPs equals 1/2 because of its direct transition nature.

The efficiency of the degradation of the CIP was measured by Acquity UPLC H−Class (Waters, America). The mobile phases of CIP consisted of MeOH and 0.1% formic acid solution (40: 60, v/v) with a flow rate of 0.2 ml/min and were used with a UV detector.

Supplementary Text 3. Photocurrent measurement

The transient photocurrent response experiments were conducted on a CHI660E electrochemical system in a three-electrode system. The sample-coated Indium tin oxide (ITO) glass, Pt wire electrode, and calomel electrode were used as the working electrode, counter electrode, and reference electrode, respectively. 0.1 M Na_2SO_4 solution was utilized as the electrolyte.

Supplementary Text 4. Photocatalytic H_2O_2 production

5 mg of photocatalyst was dispersed in 25 ml of aqueous solution. Subsequently, the dispersion was sonicated for 5 min with continuous stirring for 30 min. All photocatalytic reactions were carried out in an air atmosphere under the irradiation of a 300W xenon lamp. 1.5 ml of the solution was removed every 10 min, and the solution was filtered through a 0.45 μm filter into a centrifuge

tube. To this solution, 0.5 ml of 0.1 mol/L aqueous potassium hydrogen phthalate ($C_8H_5KO_4$) and 0.5 ml of 0.4 mol/L aqueous potassium iodide (KI) were added, and the solution was left for 3 hours. Under acidic conditions ($H_2O_2+3I^-+2H^+ \rightarrow I_3^- + 2H_2O$), H_2O_2 molecules reacted with iodide anion (I^-) to produce trivalent iodide ions (I_3^-), which have strong absorption around 350 nm. The amount of I_3^- was determined by UV-Vis spectroscopy, and the amount of H_2O_2 produced in each reaction could be estimated from the absorbance at 350 nm. A known concentration of H_2O_2 was added to a solution of KI and $C_8H_5KO_4$ and measured by UV-Vis spectrophotometer to obtain a calibration curve, see below.

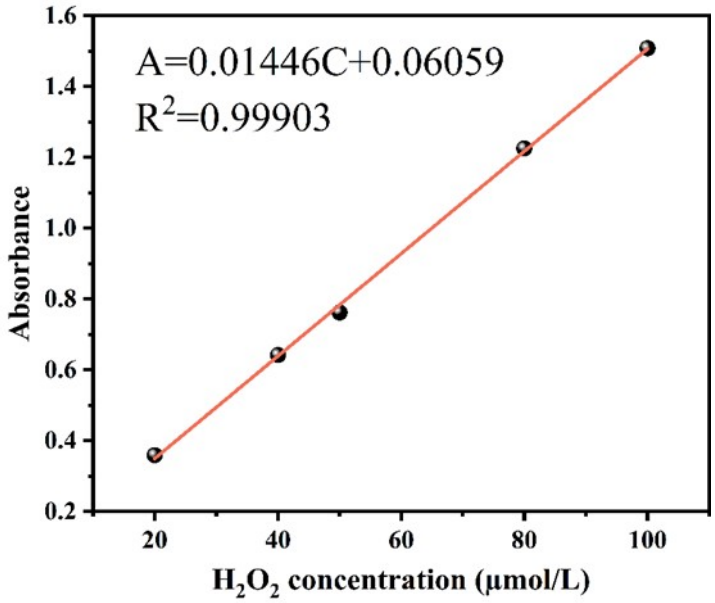

Supplementary Text 5. Apparent quantum yields (AQY) and solar-to-chemical energy conversion (SCC)

The apparent quantum yield (AQY) was measured using a monochromatic light irradiation system. A 300 W xenon lamp combined with a monochromator was used to provide light at specific wavelengths, and the incident light intensity was precisely recorded using a power meter. The AQY was calculated based on the ratio of light intensity to the number of photons absorbed, using the following formula:

$$AQY = \frac{N_{H_2O_2}}{N_p} = \frac{2N_a \times M_{H_2O_2} \times hc}{PSt\lambda} \times 100\%$$

Where M corresponds to the amount of produced H_2O_2 (mol); Na and h represent the Avogadro constant (6.022×10^{23}/mol) and Planck constant (6.626×10^{-34} J·S); c is the light velocity (3×10^8 m/s); S is the irradiation area (11.34 cm^2 in this work); P is the intensity of incident light (W/m^2); t is attributed to the reaction time (3600 s in this work); λ represents the wavelength of the incident monochromatic light (m).

λ= 380 nm:

$$AQY = \frac{2 \times 6.022 \times 10^{23} \times 1.3 \times 10^{-5} \times 6.626 \times 10 - 34 \times 3 \times 10^8}{22.1 \times 11.34 \times 10^{-4} \times 3600 \times 380 \times 10^{-9}} \times 100\% = 9.13\%$$

λ= 420 nm:

$$AQY = \frac{2 \times 6.022 \times 10^{23} \times 2.3 \times 10^{-5} \times 6.626 \times 10 - 34 \times 3 \times 10^{8}}{53.1 \times 11.34 \times 10^{-4} \times 3600 \times 420 \times 10^{-9}} \times 100\% = 6.08\%$$

λ= 450 nm:

$$AQY = \frac{2 \times 6.022 \times 10^{23} \times 3.5 \times 10^{-5} \times 6.626 \times 10 - 34 \times 3 \times 10^{8}}{76.7 \times 11.34 \times 10^{-4} \times 3600 \times 450 \times 10^{-9}} \times 100\% = 5.93\%$$

λ= 475 nm:

$$AQY = \frac{2 \times 6.022 \times 10^{23} \times 4.9 \times 10^{-5} \times 6.626 \times 10 - 34 \times 3 \times 10^{8}}{138.1 \times 11.34 \times 10^{-4} \times 3600 \times 475 \times 10^{-9}} \times 100\% = 4.36\%$$

λ= 500 nm:

$$AQY = \frac{2 \times 6.022 \times 10^{23} \times 3.6 \times 10^{-5} \times 6.626 \times 10 - 34 \times 3 \times 10^{8}}{168 \times 11.34 \times 10^{-4} \times 3600 \times 500 \times 10^{-9}} \times 100\% = 2.53\%$$

λ= 520 nm:

$$AQY = \frac{2 \times 6.022 \times 10^{23} \times 5.1 \times 10^{-5} \times 6.626 \times 10 - 34 \times 3 \times 10^{8}}{265 \times 11.34 \times 10^{-4} \times 3600 \times 520 \times 10^{-9}} \times 100\% = 2.18\%$$

The solar-to-chemical energy conversion (SCC) efficiency was determined by using an AM 1.5G solar simulator as the light source (100 mW cm^{-2}). 5 mg of catalyst and 25 ml of pure water were used for the SCC test without continuous O_2 input during the photocatalytic test.

$$\text{SCC efficiency}(\%) = \frac{\left[\Delta G \text{ for } H_2O_2 \text{ Generation}\left(J\ mol^{-1}\right)\right]\left[H_2O_2 \text{ formed}(mol)\right]}{[\text{total input power}(W)][\text{reaction time}(s)]} \times 100\%$$

where ΔG= 117 kJ mol-1. For example, when using TAPB- PMDA as the catalyst, the irradiated sample areas are 11.34 cm^2 during 1 h of sun illumination. Therefore, the calculated total input energy is 4082.4 J. During the 1 h photocatalytic reaction, x μmol H_2O_2 is generated, and the energy generated by H_2O_2 formed is 0.117x J. SCC Efficiency=0.117x/4082.4.

The optical power was determined by a PLS-SXE300D Xe lamp (Beijing Perfect Light Technology Co., Ltd., Beijing, China).

$$\text{SCC efficiency}(\%) = \frac{117000 \times 2.8 \times 10^{-4}}{1000 \times 3600 \times 11.34 \times 10^{-4}} \times 100\% = 0.81\%$$

Supplementary Text 6. Photocurrents and photoelectrochemical measurements

The Mott-Schottky plots, photocurrent response, open circuit potentials, and electrochemical impedance of the photocatalysts were measured on an electrochemical workstation (CHI660E, CHI Instruments, Shanghai, China). A 300 W Xe lamp was utilized as the light source, and Na_2SO_4 (0.5 M) aqueous solution was used as the supporting electrolyte throughout the photocurrent measurements. A platinum wire and Ag/AgCl electrode were used as counter electrode and reference electrode. 100 μL of Nafion, dry ethanol (1.0 mL) and photocatalyst (5.0 mg) were sonicated for 30 min. Then, 200 μL of the suspension was dripped onto an ITO glass substrate and dried. The application potential was converted to RHE potentials with respect to Ag/AgCl using the following equation:

$$E\ (VS.\ RHE) = E\ (VS.\ Ag/AgCl) + 0.197\ V + 0.0591 * pH$$

Supplementary Text 7. Rotating disk electrode (RDE) measurements

A glassy carbon rotating disk electrode (PINE Research Instrumentation, USA) served as the substrate for the working electrode. The working electrode was prepared as follows: 5 mg of powder

photocatalysts was dispersed in 2 mL of ethanol containing 50 μL of Nafion by ultrasonication. 20 μL of the above slurry was put onto the disk electrode and dried at room temperature. The linear sweep voltammogram (LSV) curves were recorded in an Ar or O_2-saturated 0.1 M phosphate buffer solution (pH = 7) at room temperature and a scan rate of 10 mV s^{-1} with different rotation speeds. The average number of electrons (n) was calculated by the Koutecky-Levich equation:

$$\frac{1}{J} = \frac{1}{J_L} + \frac{1}{J_K} + \frac{1}{B_{w^{1/2}}} + \frac{1}{J_K}$$

$$B = 0.62nFC_0D_0^{2/3}V^{-1/6}$$

where J is the current density, J_K and J_L are the kinetic and diffusion-limiting current densities, ω is the rotating speed (rpm), n is transferred electron number, F is Faraday constant (96485 C mol^{-1}), C_0 is the bulk concentration of O_2 (1.26×10^{-3} mol cm^{-3}), D_0 is the diffusion coefficient of O_2 (2.7×10^{-5} cm^2 s^{-1}), and *v* is kinetic viscosity of the electrolyte (0.01 cm^2 s^{-1}), respectively.

Supplementary Text 8. In-situ DRIFT measurements.

In situ diffuse reflectance infrared Fourier transform spectroscopy (DRIFTS) measurements were performed using a VERTEX 80v spectrometer (Bruker, Germany) using the KBr pellet technique. For the tests in dark conditions, the samples were filled into an in-situ IR cell, and H_2O vapor was introduced into the cell. Before the measurement, the samples were degassed at 393 K for 6 h and then purged with Ar for 1 h at 353 K. The baseline was obtained after the samples had cooled down. The tests under photocatalytic conditions were started with Ar purging for 1 h at room temperature to remove the impurities. Next, moist oxygen (a mixture of oxygen and water vapor) was introduced in the dark, and the container was sealed to stop ventilation. The adsorption process lasted for 60 min, during which data were recorded at 30 min and 60 min until oxygen adsorption equilibrium was achieved. The reaction was then initiated by turning on the 300 W Xe lamp, and data were recorded at regular intervals[2].

Supplementary Text 9. Computational Details

Quantum chemical studies were conducted using density functional theory (DFT) as implemented in GAUSSIAN 16 software package. Geometries were optimized, and frequency analyses were carried out at the B3LYP hybrid functional with GD3BJ dispersion correction, employing the def2-SVP basis sets. The adsorption energy of the various molecular fragments representing the TAPB and PMDA were determined using the following equation: $E_{ads}(AB) = E(AB) – E(A) -E(B)$. The ESP-mapped vdW surfaces and ESP extrema were rendered using the VMD 1.9.3 program based on the outputs from Multiwfn 3.8 program.

Structural characterizations of POPs.

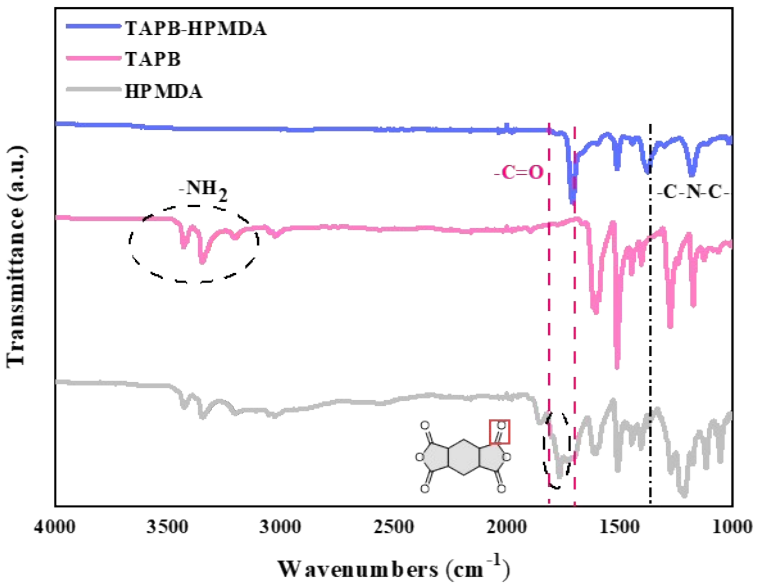

Supplementary Figure 1. FTIR spectra of the TAPB-HPMDA

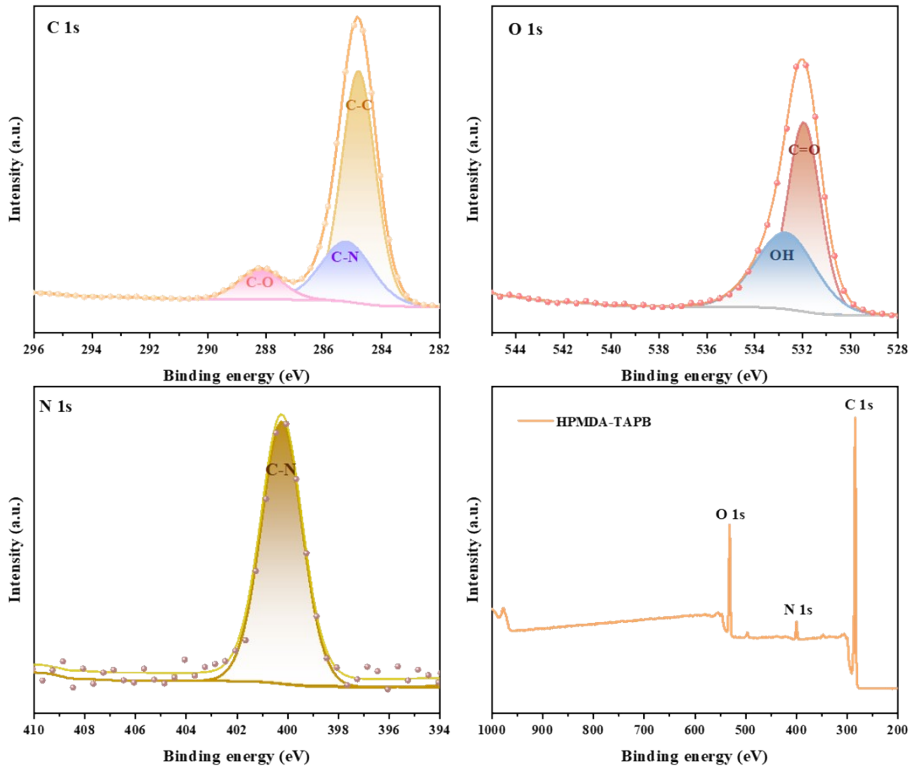

Supplementary Figure 2. XPS images of TAPB-HPMDA

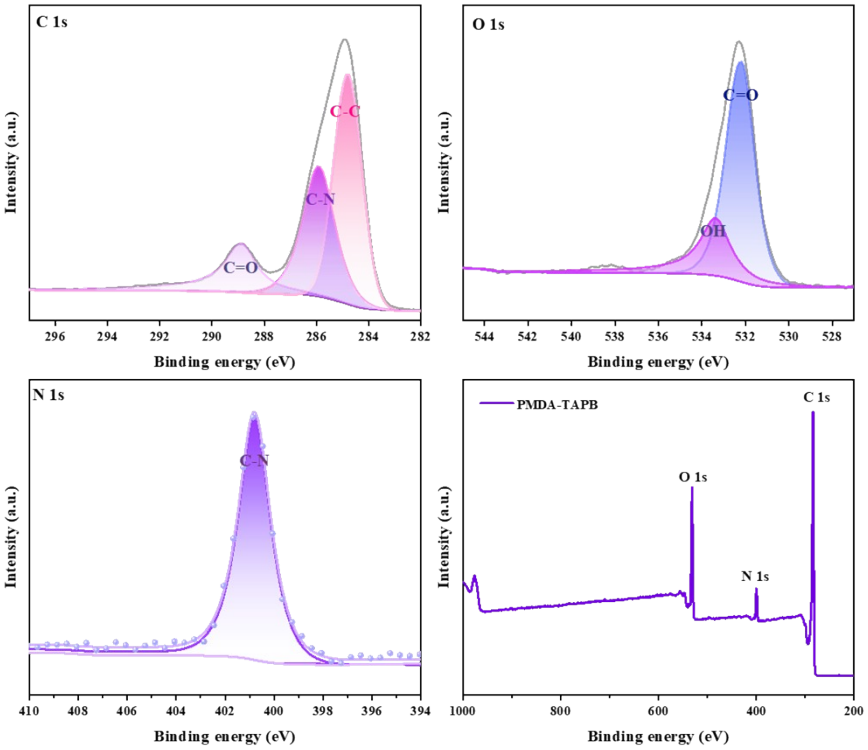

Supplementary Figure 3. XPS images of TAPB-PMDA

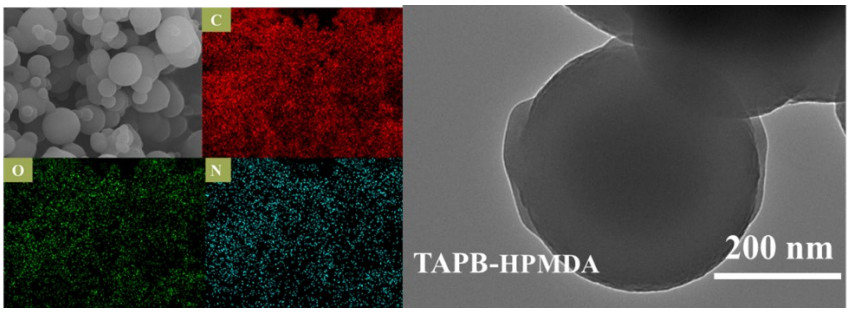

Supplementary Figure 4. SEM and TEM images of TAPB-HPMDA

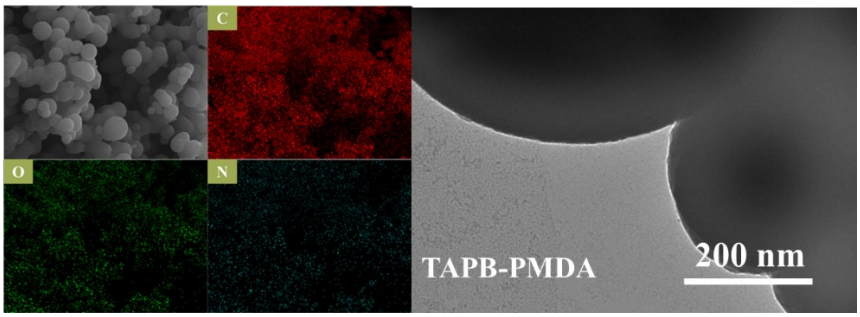

Supplementary Figure 5. SEM and TEM images of TAPB-PMDA

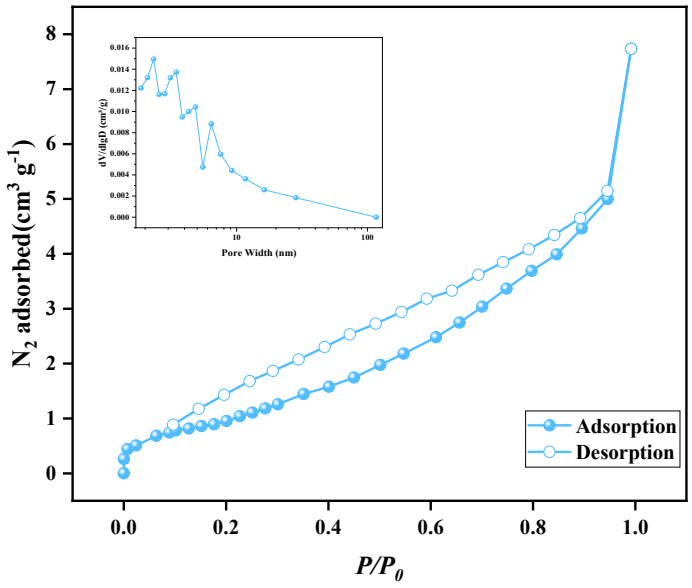

Supplementary Figure 6. N_2 adsorption-desorption isotherm and pore size distribution (inset) of TAPB-HPMDA

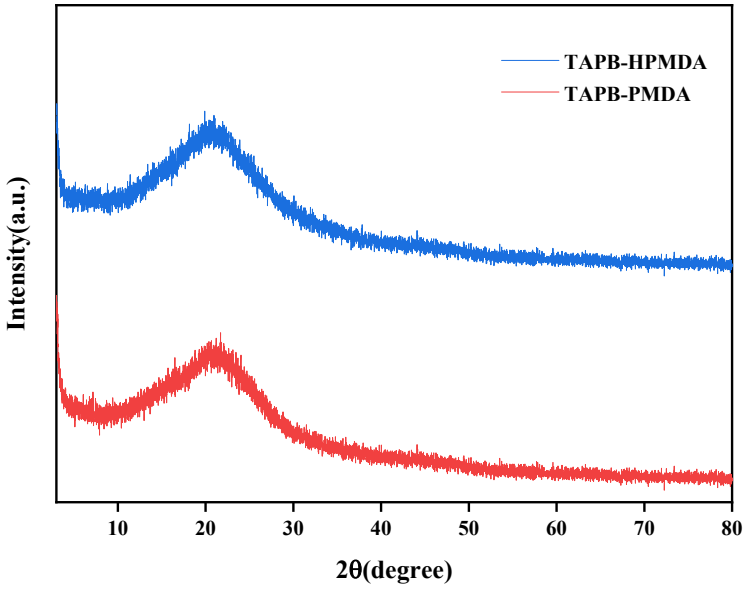

Supplementary Figure 7. XRD images of POPs

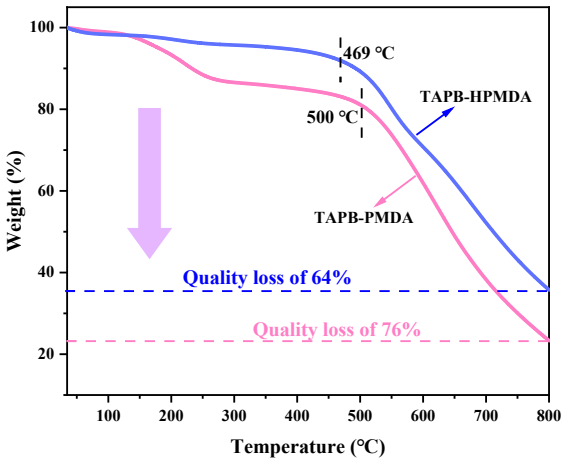

Supplementary Figure 8. TG plot of POPs.

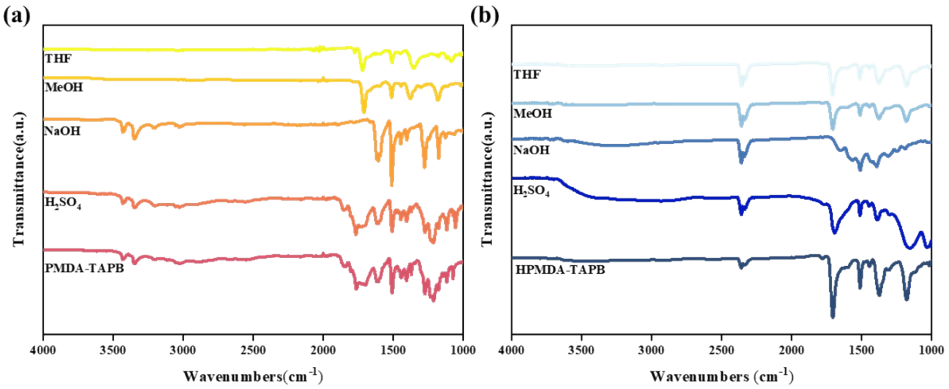

Supplementary Figure 9. FT-IR plots of (a) TAPB-PMDA and (b) TAPB-HPMDA after being immersed in THF, MeOH, NaOH, and H_2SO_4

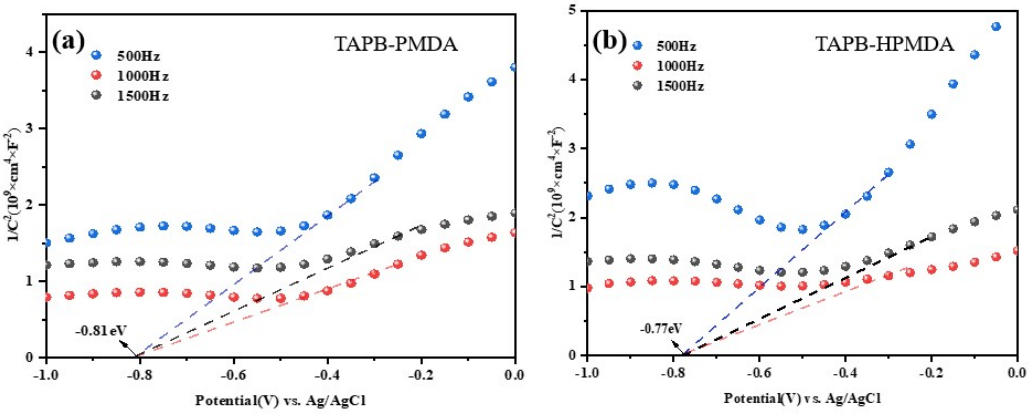

Supplementary Figure 10. Mott-Schottky plots of POPs

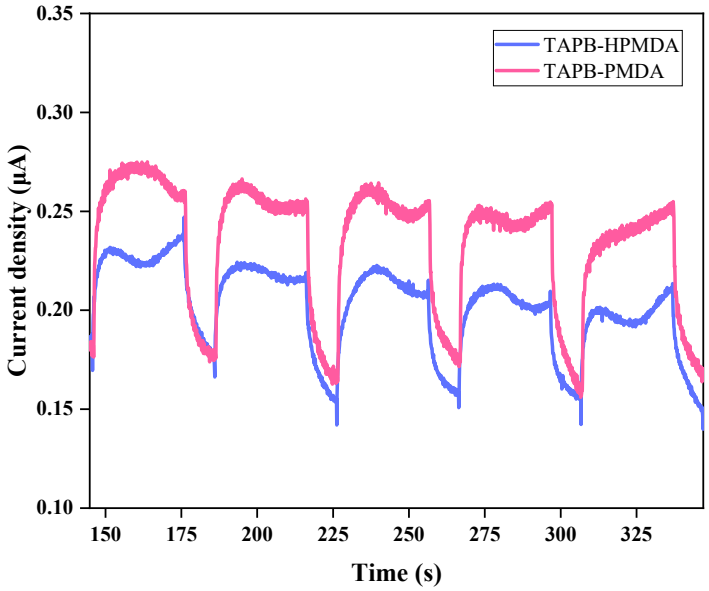

Supplementary Figure 11. Transient photocurrent densities of POPs

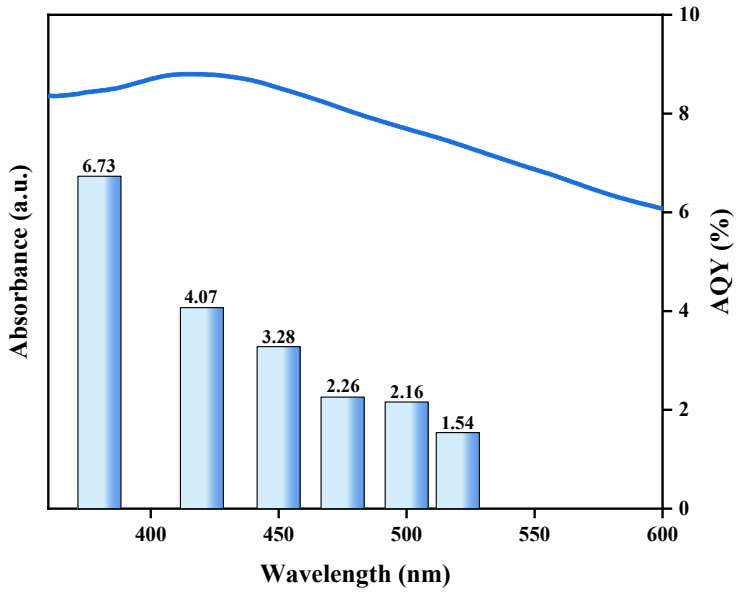

Supplementary Figure 12. AQY spectra of TAPB-HPMDA.

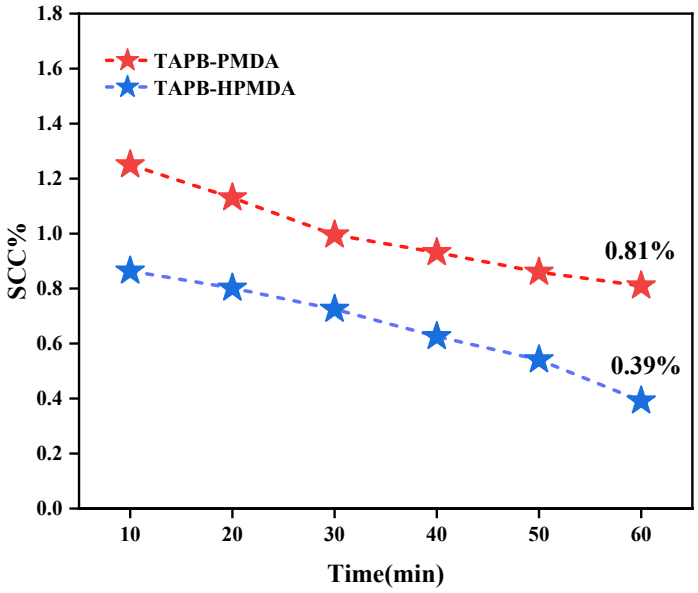

Supplementary Figure 13. SCC of TAPB-HPMDA and TAPB-PMDA.

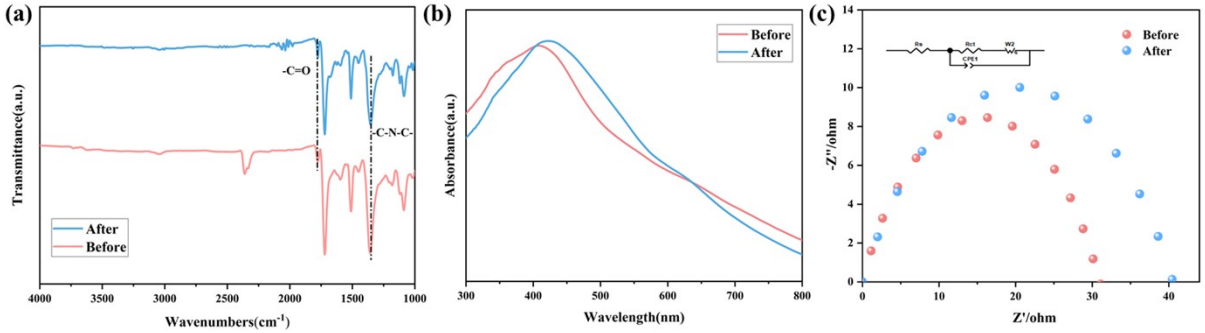

Supplementary Figure 14. (a) FTIR spectra before and after the cycle, (b) UV-vis spectra before and after the cycle, (c) EIS spectra before and after the cycle

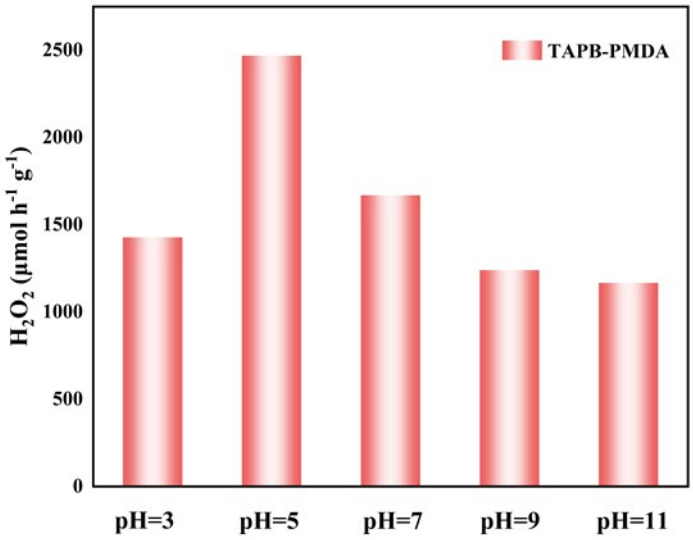

Supplementary Figure 15. The effect of solution pH on the photocatalytic H_2O_2 production by TAPB-PMDA

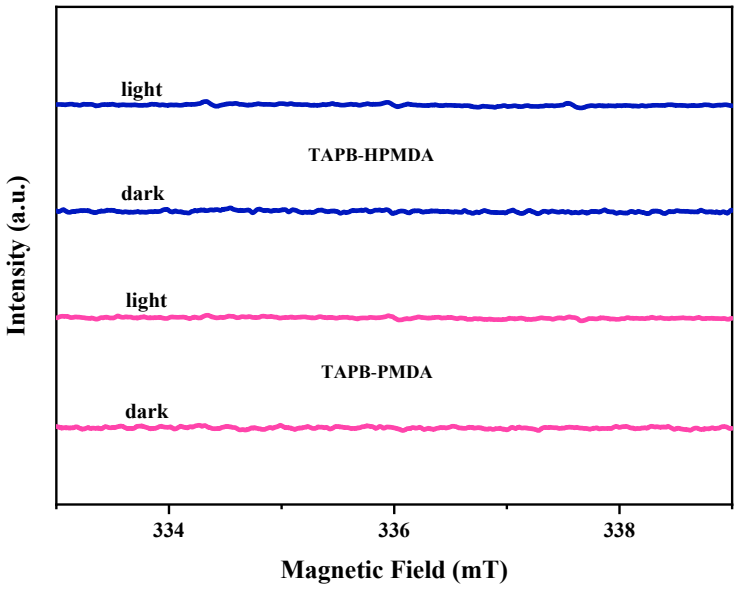

Supplementary Figure 16. EPR spectra of $^1O_2$.

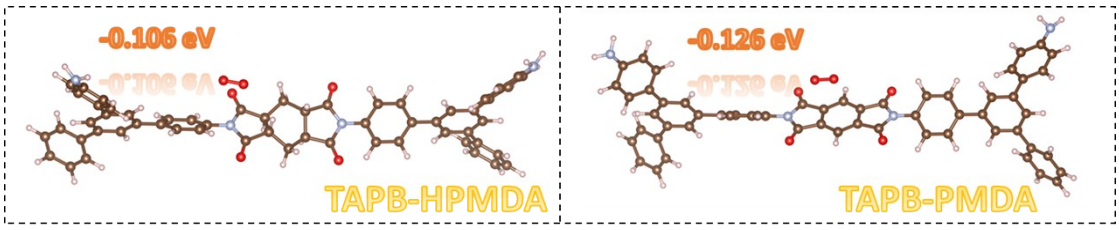

Supplementary Figure 17. Adsorption sites of oxygen during the oxygen reduction reaction (ORR)

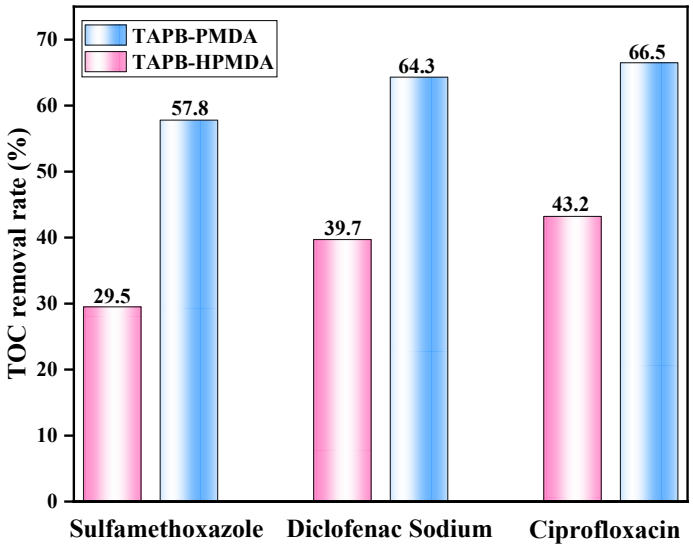

Supplementary Figure 18. TOC removal rate of TAPB-HPMDA and TAPB-PMDA.

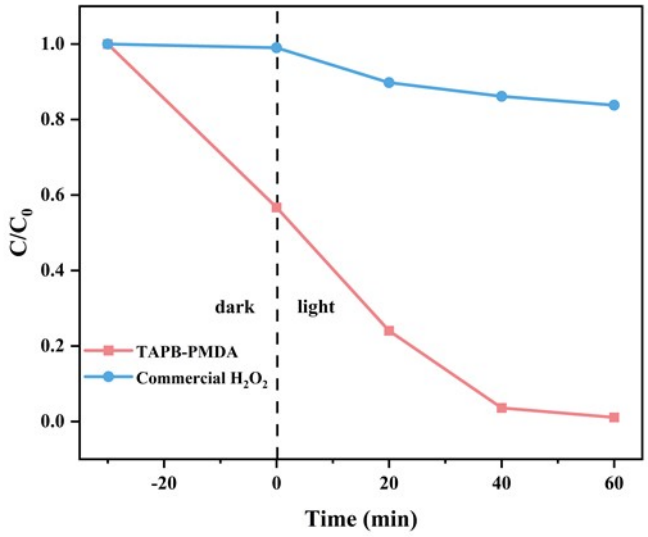

Supplementary Figure 19. Control experiments on the degradation of CIP with the addition of commercial H_2O_2

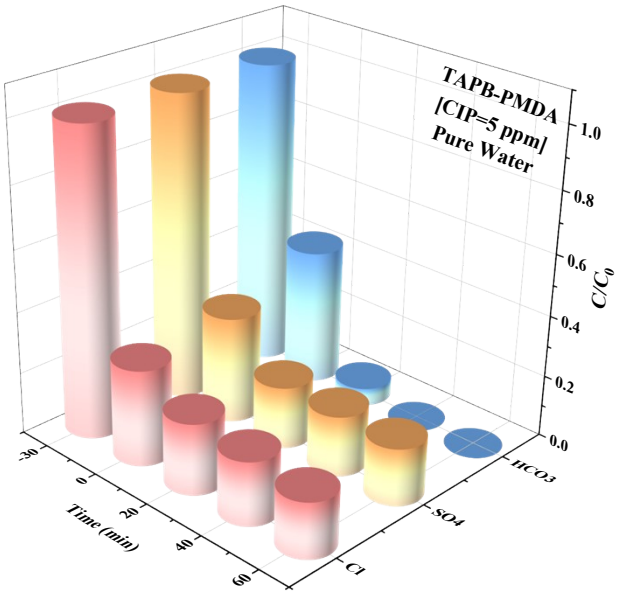

Supplementary Figure 20. CIP removal efficiency and rate constants (inset) by TAPB-PMDA in pure water containing coexisting anions

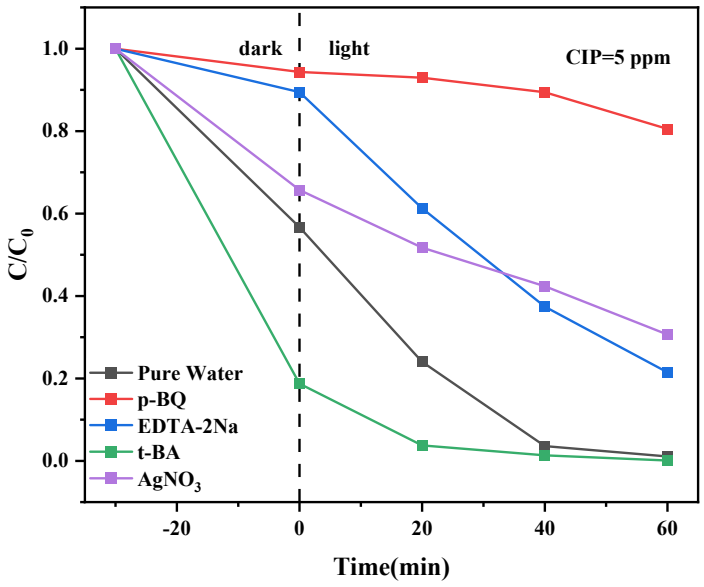

Supplementary Figure 21. Radical quenching experiments of CIP degradation by TAPB-PMDA

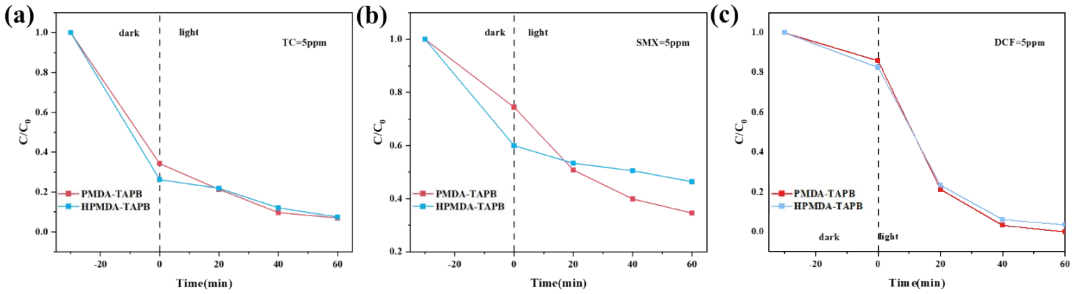

Supplementary Figure 22.TC, SMX, and DCF removal efficiencies by TAPB-PMDA and TAPB-HPMDA

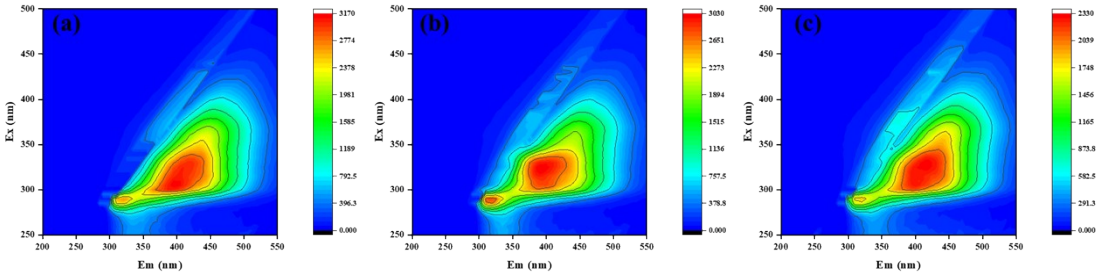

Supplementary Figure 23. 3D EEM spectra of (a) solution before treatment of landfill leachate, (b) solution after degradation by TAPB-PMDA, (c) solution after degradation by TAPB-HPMDA

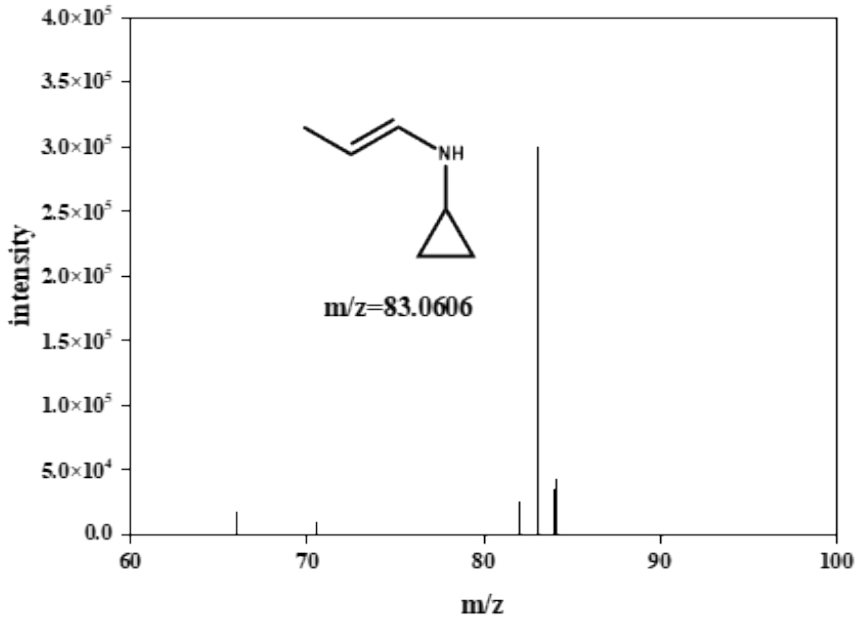

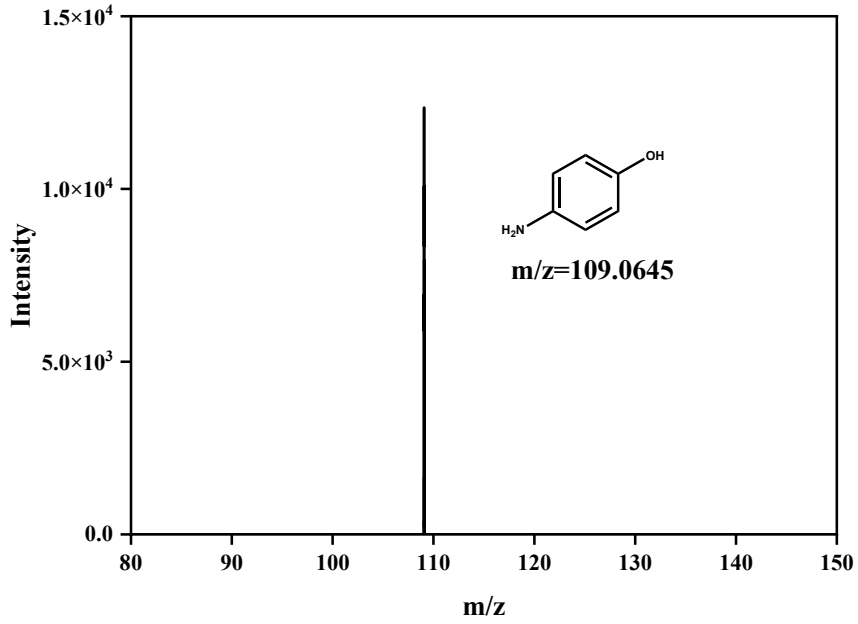
1.5×10^4
1.0×10^4
5.0×10^3
0.0
Intensity
80
90
100
110
120
130
140
150
m/z
OH
H2N
m/z=109.0645

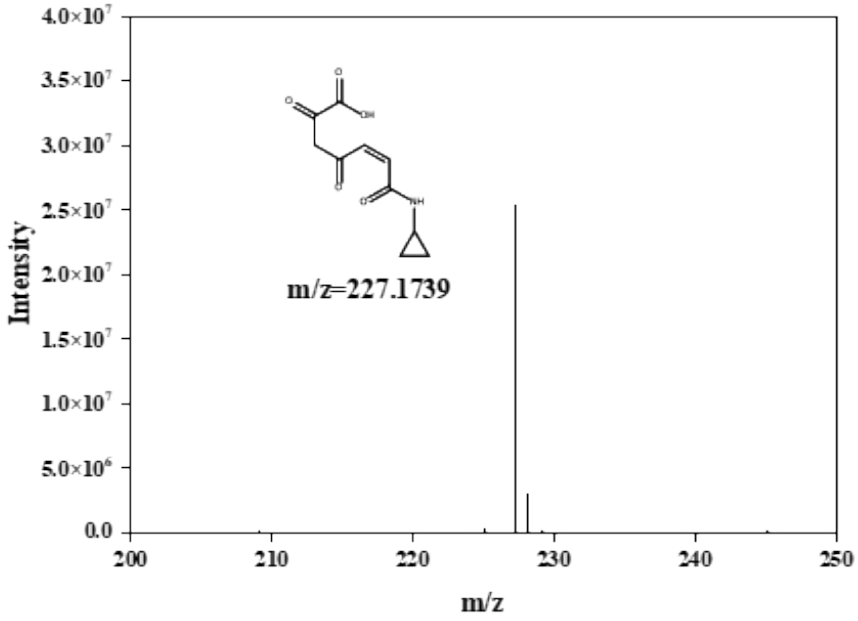
4.0×10^7
3.5×10^7
3.0×10^7
2.5×10^7
2.0×10^7
1.5×10^7
1.0×10^7
5.0×10^6
0.0
Intensity
200
210
220
230
240
250
m/z
m/z=227.1739

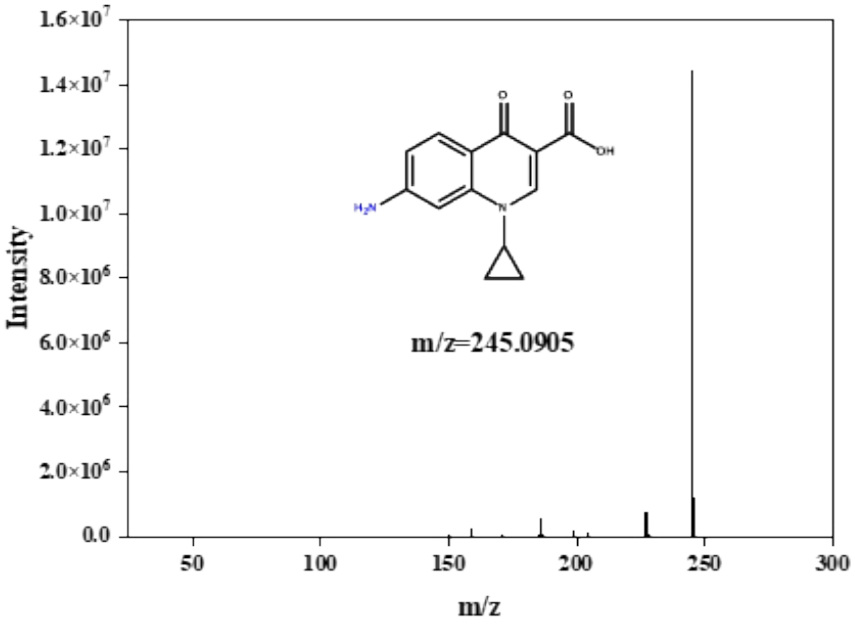
Intensity
m/z
m/z=245.0905

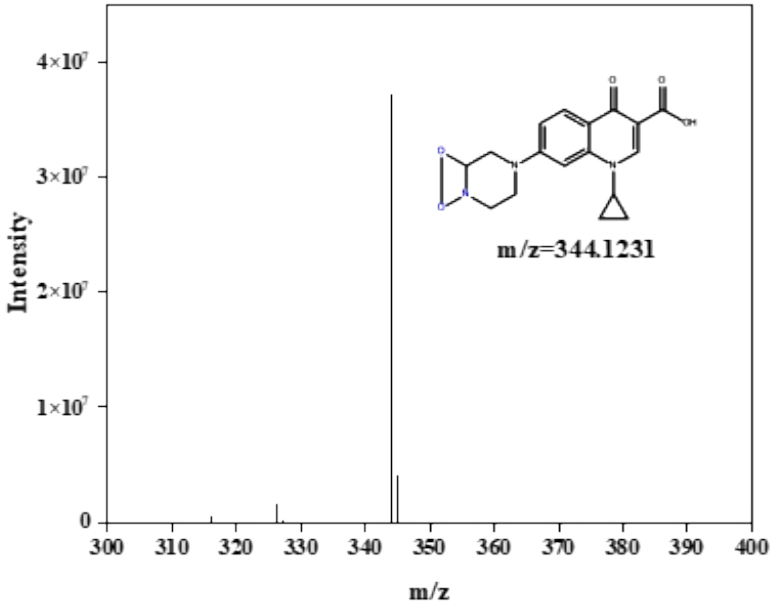
Intensity
m/z
m/z=344.1231

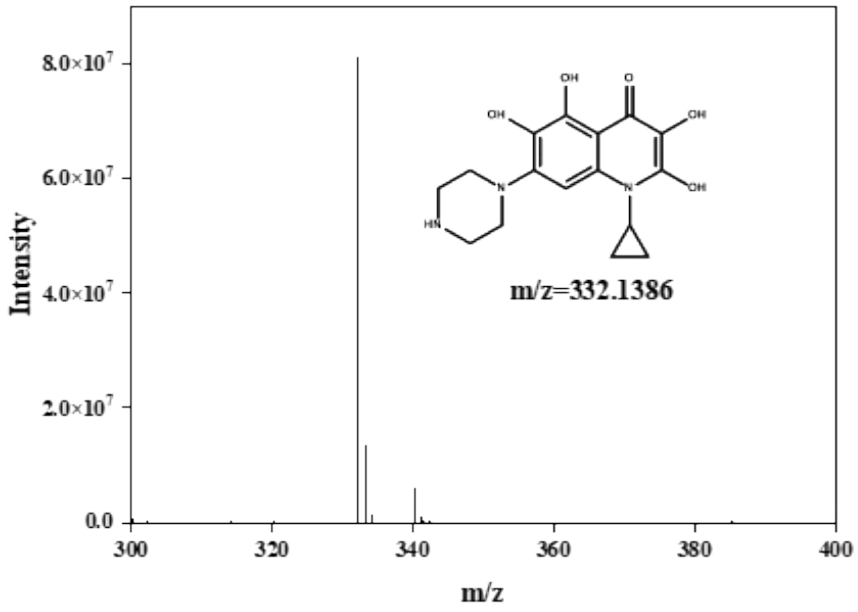

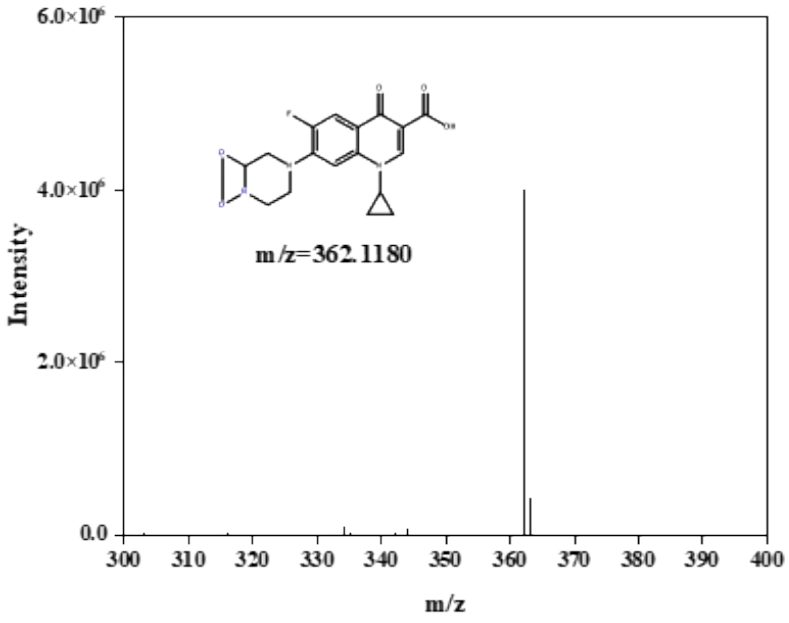

Supplementary Figure 24. LC-MS of CIP by TAPB-PMDA

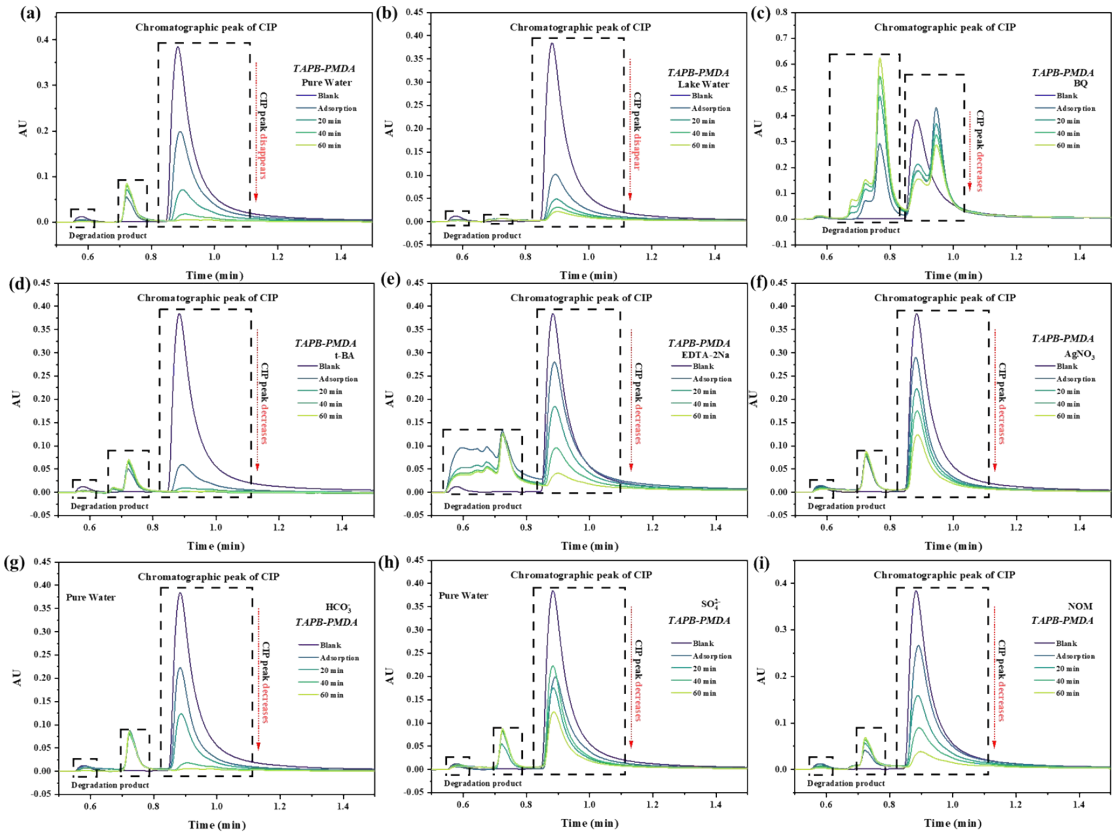

Supplementary Figure 25. UPLC chromatograms of CIP degradation by TAPB-PMDA in pure water, lake water, and radical quenching experiments of TAPB-PMDA.

Table S1. The BET specific surface area, pore volume, and average aperture of TAPB-PMDA and TAPB-HPMDA

BET	**Specific surface area**	**Pore volume**	**Average aperture**
TAPB-HPMDA	7.07 m^2/g	0.0118 cm^3/g	9.7737 nm
TAPB-PMDA	385.90 m^2/g	0.1627 cm^3/g	2.1938 nm

Table S2. Dissolved oxygen concentration (mg/L) in deionized water and oxygen-exposed deionized water

	Deionized water	**Oxygen-exposed deionized water**
Dissolved oxygen（mg/L）	4.53	8.61

Table S3. Comparison of H_2O_2 production performance of POP photocatalysts.

Photocatalyst	H_2O_2 yield	AQY	SCC	Ref.
TAPB-PMDA	**2440.74 μmol g^{-1} h^{-1}**	**9.13% at 380nm**	**0.81%**	**This work**
CHF-DPDA	1725 μmol g^{-1} h^{-1}	16% at 420nm	0.78%	[3]
TapbBtt-COF	1400 μmol g^{-1} h^{-1}	4.6% at 450nm	0.29%	[4]
TT-DTDA-COF	1302 μmol g^{-1} h^{-1}	3.02% at 400nm	0.17%	[5]
COF-BTT-TAPT	620.2 μmol g^{-1} h^{-1}	0.15% at 420nm	/	[6]
Cu3-BT-COF	1870 μmol g^{-1} h^{-1}	7.98% at 420 nm	0.62%	[7]
DVA-COF	3760 μmol g^{-1} h^{-1}	2.84% at 420 nm	0.08%	[8]
MIL-125-NH_2	748 μmol g^{-1} h^{-1}	3.1% at 365 nm	/	[9]
PQ-AB	3400 μmol g^{-1} h^{-1}	5.02% at 400 nm	0.2%	[10]
C4N/MgAl-LDH	2380 μmol g^{-1} h^{-1}	3.26% at 420 nm	/	[11]
CoOx/Mo:BiVO4 /Pd	712.5 μmol g^{-1} h^{-1}	5.8% at 420 nm	0.29%	[12]

Table S4. Comparison of H_2O_2 production performance of representative COFs, POPs, and organic-polymer-based photocatalysts.

Photocatalyst	Structural feature	H_2O_2 yield	AQY	SCC	Ref.
TAPB-PMDA	**imide-linked POP**	**2440.74 μmol g^{-1} h^{-1}**	**9.13% at 380nm**	**0.81%**	**This work**
P-TDZ	imide-linked	2177 μmol g^{-1} h^{-1}	2.91% at 420nm	0.11%	[13]
PB-COF	imide-linked COF	2044 μmol g^{-1} h^{-1}	9.8% at 420nm	0.68%	[14]
PI-BD-TPB	imide-linked aerogel photocatalyst	2632.88 μmol g^{-1} h^{-1}	14.28% at 420nm	0.92%	[15]
CQD-CTF	carbon quantum dots confined in CTF	1036 μmol g^{-1} h^{-1}	1.03% at 420 nm	0.21%	[16]
Polyimide/$ZnIn_2S_4$	Polyimide heterostructure	411.07 μmol g^{-1} h^{-1}	0.081% at 400 nm	/	[17]

Table S5. The test data of COD, TP, TN, and NH_4^+-N of Minghu Lake and Tap water

Sample	COD (mg/L)	TP (mg/L)	TN (mg/L)	NH_4^+-N (mg/L)
Minghu Lake	17.68	0.014	0.637	0.087
Tap water	0.32	0.004	1.162	0.000

Table S6. Electrical conductivity (μS/cm) of water samples with inorganic ions added.

	Cl^-	SO_4^{2-}	HCO_3^-
Electrical conductivity (μS/cm)	103	255	93.8

Table S7. Scope of Toxicity Assessment

Toxicity rang(mg/L)	Logarithmic-transformed toxicity range	Class
$k \leq 1$	$\lg k \leq 0$	Very toxic
$1 < k \leq 10$	$0 < \lg k \leq 1$	Toxic
$10 < k \leq 100$	$1 < \lg k \leq 2$	Harmful
$k > 100$	$\lg k > 2$	Not harmful

References

[1] Chi W, Liu B, Dong Y, et al. Boosting H_2O_2 photosynthesis by accumulating photo-electrons on carbonyl active site of polyimide covalent organic frameworks[J]. Applied Catalysis B: Environment and Energy, 2024, 355: 124077.

[2] Liu C, Liu X, Chen B, et al. Squaric acid-based zwitterionic covalent organic framework induces triple synergy for boosted hydrogen peroxide photosynthesis[J]. Nature Communications, 2025, 16(1): 8941.

[3] Cheng H, Lv H, Cheng J, et al. Rational design of covalent heptazine frameworks with spatially separated redox centers for high-efficiency photocatalytic hydrogen peroxide production[J]. Advanced Materials, 2022, 34(7): 2107480.

[4] Qin C, Wu X, Tang L, et al. Dual donor-acceptor covalent organic frameworks for hydrogen peroxide photosynthesis[J]. Nature Communications, 2023, 14(1): 5238.

[5] Wang Y, Zhao H, Li P, et al. Asymmetric acceptor-donor-acceptor type covalent organic frameworks with dual O_2 reduction moieties for boosting H_2O_2 photosynthesis[J]. Chemical Engineering Journal, 2024, 491: 151825.

[6] Liu M, He P, Gong H, et al. Benzotrithiophene-based covalent organic frameworks as efficient catalysts for artificial photosynthesis of H_2O_2 in pure water[J]. Chemical Engineering Journal, 2024, 482: 148922.

[7] J.-N. Chang, J.-W. Shi, Q. Li, S. Li, et al. Regulation of redox molecular junctions in covalent organic frameworks for H_2O_2 photosynthesis coupled with biomass valorization[J]. Angew. Chem. Int. Ed. 2023, 62, e202303606.

[8] H. Yu, F. Zhang, Q. Chen, P.-K. Zhou, et al. Vinyl-group-anchored covalent organic framework for promoting the photocatalytic generation of hydrogen peroxide[J]. Angew. Chem. Int. Ed. 2024, 63, e202402297.

[9] L. Yuan, P. Du, C. Zhang, et al. Facet-dependent spatial separation of dual cocatalysts on MOF photocatalysts for H_2O_2 production coupling biomass oxidation with enhanced performance[J]. Appl. Catal. B Environ. Energy 2025, 364, 124855.

[10] X. Sun, T. Yang, Y. Dong, et al. Phenanthrenequinone-modified conjugated polymer enabling photocatalytic H_2O_2 generation via efficient O_2-conversion[J]. Adv.

Energy Mater. 2025, 15, 2405687.

[11] Y. Teng, X.-M. Zhang, R.-L. Zhu, et al. Interface-engineered C_4N/MgAl-LDH heterostructure for high-performance photocatalytic H_2O_2 production[J]. Angew. Chem. Int. Ed. 2025, e202516296.

[12] T. Liu, Z. Pan, J. J. M. Vequizo, et al. Overall photosynthesis of H_2O_2 by an inorganic semiconductor[J]. Nat. Commun. 2022, 13, 1034.

[13] Xiong K, Lin X, Li S, et al. Rapid Preparation of DA Microporous Polyimides via Domino Polymerization for Photocatalytic Hydrogen Peroxide Production[J]. ACS Macro Letters, 2025, 14(9): 1307-1313.

[14] Chi W, Liu B, Dong Y, et al. Boosting H_2O_2 photosynthesis by accumulating photo-electrons on carbonyl active site of polyimide covalent organic frameworks[J]. Applied Catalysis B: Environment and Energy, 2024, 355: 124077.

[15] Chi W, Dong Y, Liu B, et al. A photocatalytic redox cycle over a polyimide catalyst drives efficient solar-to-H_2O_2 conversion[J]. Nature Communications, 2024, 15(1): 5316.

[16] Yang Y, Guo Q, Li Q, et al. Carbon quantum dots confined into covalent triazine frameworks for efficient overall photocatalytic H_2O_2 production[J]. Advanced Functional Materials, 2024, 34(29): 2400612.

[17] Liu X, Dong X, Wang Y, et al. Polyimide/$ZnIn_2S_4$ heterostructures toward outstanding photocatalytic H_2O_2 production from pure water and air[J]. Applied Surface Science, 2024, 643: 158637.